AGU PUBLICATIONS

JGR

Journal of Geophysical Research: Space Physics

RESEARCH ARTICLE
10.1002/2016JA022395

Mass loading at the magnetopause through the plasmaspheric plume

Yan Wang[1], Jiannan Tu[1], and Paul Song[1]

[1] Space Science Laboratory and Physics Department, University of Massachusetts Lowell, Lowell, Massachusetts, USA

Key Points:
- The plasmaspheric plumes greatly enhance the equatorial magnetopause plasma density
- The higher density can be further enhanced by the wave-particle interaction
- The dayside reconnection rate may be substantially reduced in association with the plumes

Correspondence to:
Y. Wang,
Yan_Wang@student.uml.edu

Citation:
Wang, Y., J. Tu, and P. Song (2016), Mass Loading at the magnetopause through the plasmaspheric plume, *J. Geophys. Res. Space Physics*, *121*, doi:10.1002/2016JA022395.

Received 15 JAN 2016
Accepted 17 SEP 2016
Accepted article online 23 SEP 2016

Abstract An investigation of the transport of the plasmaspheric plasma to the dayside magnetopause under disturbed geomagnetic conditions associated with plasmaspheric plumes is conducted by numerical simulations using the Dynamic Fluid-Kinetic (DyFK) model. The simulations present the field-aligned density distributions and kinetic features of multiple ion species ($H^+/He^+/O^+$) in a plasmaspheric flux tube that corotates while convecting toward the dayside magnetopause. The simulations show that the plasmaspheric plume can provide an equatorial magnetopause plasma density which is up to 3 orders of magnitude higher than that under the typical conditions. With the effects of wave-particle interaction included, such mass loading through the plasmaspheric plume is even stronger. The local reconnection rate at the location where the plasmaspheric plume mass loads at the dayside magnetopause may decrease by 90%, depending on the geomagnetic activities, the outer plasmaspheric density, and the level and spatial span of the wave-particle interaction.

1. Introduction

The Earth's plasmasphere is a region of cold (<1 eV) and relatively dense ($10^2 \sim 10^4$ cm^{-3}) plasma, bounded by a sharp density decrease (plasmapause) on the outer side. Its configuration is very dynamic and depends on the history of the geomagnetic activity. During prolonged geomagnetic quiet period, the plasmasphere can extend beyond geosynchronous orbit [e.g., *Tu et al.*, 2006, 2007]. During active periods, the flux tubes in the outer plasmasphere, which originally follow closed drift paths corotating with the Earth, now follow open drift paths to move toward the dayside magnetopause due to the enhanced magnetospheric convection. These flux tubes newly on the open drift paths form a plasmaspheric drainage plume, which is a region of high density (up to $\sim$ 100 cm^{-3}) compared to its surroundings in the plasma trough (0.1 $\sim$ 10 cm^{-3}) and consists of various low-energy terrestrial ion species (primarily H^+ with a variable fraction of O^+ and He^+ ions) [cf. *Borovsky and Denton*, 2008; *Darrouzet et al.*, 2008, 2009, and references therein]. The plasmaspheric plumes have been observed by a number of satellites against the magnetopause [e.g., *Elphic et al.*, 1996] and shown to possibly have significant effects on dayside magnetic reconnection and solar wind-magnetosphere coupling [e.g., *Su et al.*, 2000; *Cassak and Shay*, 2007; *Borovsky and Denton*, 2006; *Borovsky et al.*, 2008; *McFadden et al.*, 2008; *Walsh et al.*, 2013, 2014a, 2014b]. *Borovsky and Denton* [2006] indicated that a weakened coupling of the solar wind to the magnetosphere may be caused by the plasmaspheric plume via statistically analyzing the measured geomagnetic indices. *Cassak and Shay* [2007] have derived an expression showing that the reconnection rate is dependent on the mass densities in both the magnetosheath and the magnetopause. A global MHD simulation showed that the reconnection rate decreased when the plasma density increased [*Borovsky et al.*, 2008]. *Walsh et al.* [2014a] found that the reconnection jet velocity was slower when the plume was present than when the plume was absent, indicating less efficient reconnection due to the presence of the high-density plume.

The structures of the plasmaspheric plumes have been studied by a large number of observations and simulations for decades [e.g., *Grebowsky*, 1970; *Chen and Wolf*, 1972; *Elphic et al.*, 1996; *Moldwin*, 1997; *Spasojević et al.*, 2003; *Pierrard and Lemaire*, 2004; *Goldstein et al.*, 2005; *Walsh et al.*, 2013; *Lee et al.*, 2016]. However, there is less knowledge about the ion compositions in the plasmasphere. In MHD simulations the plasmaspheric plasma is treated as a single species. In observations, composition measurements are rare [*Fraser et al.*, 2005; *Takahashi et al.*, 2008]. On the other hand, the plasmaspheric particles are of Earth's origin with many heavy ions which react differently with the changing conditions. In the simulation of the plasmaspheric refilling, lighter ion particles (H^+ and He^+) are more likely to reach the equator and form interhemispherical flow and

equatorial trapping, whereas the heavier ones (O^+) are less likely to accumulate in a large quantity in the lower latitudes [*Wang et al.*, 2015].

Wang et al. [2015] have developed a new dynamic fluid-kinetic (DyFK) model which couples a multispecies particle code with a fluid ionosphere to simulate the transport between the ionosphere and plasmasphere as well as the dynamics. The flux tube in the DyFK model is allowed to move both azimuthally around the Earth and radially from near the Earth to the magnetopause, which may result in expansion in its length and cross-sectional area. Although several numerical models were capable of simulating the plasma transport along the flux tube in association with the magnetospheric convection [e.g., *Rasmussen et al.*, 1993; *Miller et al.*, 1993; *Huba et al.*, 2000], the DyFK model is the only existing plasmasphere simulation model that not only self-consistently couples kinetic treatments for multiple ion species ($O^+/H^+/He^+$) with realistic ionospheric conditions but also includes effects of the flux tube convection. The simulation results from the DyFK model are able to provide the ion compositions in the plumes as well as their field-aligned density distributions. The effect of the plasmaspheric mass loading at the magnetopause on reconnection may be more prominent if the plume contains enhanced heavy (He^+ and/or O^+) ion population. Therefore, the quantitative information provided by the simulation results from the new DyFK model about the mass loading through the plasmaspheric plume to the dayside magnetopause will be greatly beneficial to the understanding of the solar wind and magnetosphere coupling. In the next section, we describe this numerical model and the algorithm of the wave-particle interaction. Section 3 presents the simulation results of the mass loading of the plasmaspheric plasma at the dayside magnetopause and the effects of the wave-particle interaction on the plasma transport. A summary and discussion are given in section 4.

2. Simulation Method

2.1. The Numerical Model

The new Dynamic Fluid-Kinetic (DyFK) model is used to study the plasma transport to the dayside magnetopause in association with the plasmaspheric plume due to enhanced magnetospheric convection. The new DyFK model couples the field line interhemispheric plasma (FLIP) model with a semikinetic approach via an overlapped transition region (800 km – 1100 km altitude) in each of the hemispheres to investigate the plasma transport along closed magnetic field lines (schematically shown in Figure 1 of *Wang et al.* [2015]). The FLIP model, which has been extensively used in the ionosphere and plasmasphere simulation, solves time-dependent mass, momentum, and energy transport equations along a closed magnetic field line above 120 km altitude, including comprehensive chemistry for O^+, H^+, He^+, N^+, and electrons [*Richards and Torr*, 1990; *Richards et al.*, 2000]. The ion momentum equations in the FLIP model are solved with the inertial terms ignored. The FLIP model is truncated at 1100 km altitude in both hemispheres and used as the ionospheric part, where the plasma density is very high and collisions are dominant. On the other hand, ions ($O^+/H^+/He^+$) and electrons are treated as simulation particles and a fluid in the semikinetic domain of the DyFK model (above 800 km altitude). Each simulation particle moving along the magnetic field line is subjected to the field-aligned electric field, gravitational force, magnetic mirror force, centrifugal force, and interspecies and intraspecies Coulomb collisions. The electron density and velocity are derived from the quasi-neutrality and parallel current-free conditions, respectively. The electron temperature is assumed to be isotropic and given by an empirical model derived by *Titheridge* [1998]. A more comprehensive electron temperature calculation will be included [e.g., *Liemohn et al.*, 1997] in future works. The simulation results provide magnetic field-aligned distributions of densities, flow velocities, anisotropic temperatures for multiple ion species ($H^+/He^+/O^+$), and ion velocity distributions in the phase space.

Although the semikinetic approach in the DyFK model is developed based on the generalized semikinetic (GSK) model [*Wilson et al.*, 1992], it additionally treats ion species O^+ and He^+ as simulation particles and includes the geometrical change of the flux tube associated with the meridional magnetospheric convection. Heavy O^+ ions demonstrated different behaviors compared to lighter H^+ and He^+ ions during plasmaspheric refilling [*Wang et al.*, 2015]. The He^+ distribution is also of interest because some of the plasmaspheric ultraviolet (EUV) images are taken from He^+ resonance emission lines at 30.4 nm. In addition, an important feature, as the flux tube convects away from the Earth toward the dayside magnetopause, is that the high-density ionosphere appears to rise. The lower boundary of the semikinetic domain is fixed at 800 km altitude in both hemispheres during the flux tube convection. If the flux tube convects poleward, the grid points at the lower boundary of the semikinetic domain in both hemispheres rise to an altitude above 800 km altitude and the flux tube intersects the 800 km altitude surface at two new points. Therefore, additional portion of

the flux tube is "pulled out" of the ionosphere in the semikinetic domain. Such effect described in section 2.4 of *Wang et al.* [2015] in detail is for the first time included in a numerical simulation model of the inner magnetosphere.

The fluid and semikinetic treatments in the DyFK model are coupled as follows. The bulk parameters (densities, velocities, parallel and perpendicular temperatures, and parallel and perpendicular heat fluxes) in the semikinetic domain and their gradients are passed to the fluid domain at 1100 km as the upper boundary conditions of the fluid equations. The densities, field-aligned flow velocities, and temperatures from the fluid treatment at 800 km altitude in both hemispheres are taken as input parameters for gyro-averaged drift Maxwellian velocity distributions of three ion species (O^+, H^+, and He^+). The simulation particles with upward velocities in these velocity distributions are then injected into the semikinetic domain at 800 km altitude in both hemispheres. The overlapped region (800 km – 1100 km in altitude) allows dynamic adjustments in the parameters in both simulation domains in order to maintain a smooth connection between the solutions from the two parts of the coupled model. Further details of the DyFK model can be found in *Wang et al.* [2015].

2.2. Drift Trajectory of the Flux Tube

In the present study, the flux tubes in the outer plasmasphere follow the $\mathbf{E} \times \mathbf{B}$ drift trajectories under the enhanced magnetospheric convection from an initially closed drift path to an open one. The specific mechanism of the plasmaspheric plume formation is beyond the scope of the present study, although a couple of mechanisms have been proposed, which are the time-varying convection electric field [*Chen and Wolf*, 1972; *Spiro et al.*, 1981; *Lambour et al.*, 1997] and interchange instability [*Pierrard and Lemaire*, 2004]. For cold plasmaspheric ions (<1 eV), only $\mathbf{E} \times \mathbf{B}$ drift is included, ignoring the curvature and gradient drifts. We adopt the *McIlwain E5D* magnetospheric convection electric potential model [*McIlwain*, 1986] with the corotation electric potential included to calculate the drift trajectory of a flux tube in the equatorial plane. *McIlwain* [1986] derived an analytical representation (E5D model) of the convection electrostatic potential at the equator of the magnetosphere based on ATS-5 and ATS-6 observations at geosynchronous orbit. The McIlwain E5D model depends on the radial distance, local time, and 3-hourly geomagnetic activity index *Kp* and is not driven by the solar wind parameters. *Pierrard et al.* [2008] have shown that the McIlwain E5D electric field model performs better than other electric field models in representing the plasmapause location, the plasmaspheric plume location, and shape. We use the static dipole magnetic field for a zero-order approximation in this study and more realistic magnetic field models (e.g., *Tsyganenko* [1995] magnetic field model) will be utilized in future works.

2.3. Algorithm of Wave-Particle Interaction

Previous studies have shown that the wave-particle interaction may have significant influences on the plasma transport in the inner magnetosphere [e.g., *Singh and Hwang*, 1987; *Lin et al.*, 1992; *Singh and Horwitz*, 1992]. Broadband electromagnetic ion cyclotron (EMIC) waves are of particular importance in the context of the wave-particle interaction in the plasma transport since the frequency range of these waves encompasses gyrofrequencies of the O^+, He^+, and H^+ ions and the waves can resonantly interact with these ions. In the present simulations, we consider how the wave-particle interaction, specifically, the ion heating by broadband EMIC waves, may affect the plasmaspheric ion transport to the magnetopause. We utilize a parameterized method, which was used in *Lin et al.* [1992], to simulate the ion heating by the waves in the flux tube. *Lin et al.* [1992] used the original GSK model with fixed upward ionospheric fluxes at the geocentric distance 1.3 R_E to investigate effects of the wave-particle interaction on H^+ refilling processes along an initially depleted flux tube. The ion resonantly interacts with the particular EMIC wave whose Doppler-shifted frequency is the harmonics of the ion gyrofrequency. During each time step, Δt, the net change in the gyrospeed of the ion is $\Delta v_\perp = \left(q_i \delta E_\perp / m_i\right) \Delta t$ [*Chang et al.*, 1986], where $\delta E_\perp$ is the perpendicular electric field strength of the wave and q_i and m_i are the charge and mass of the ion particle, respectively.

The perpendicular energy of an ion particle, $W_\perp = \frac{1}{2} m_i v_\perp^2$, is first calculated through the conservation of the magnetic moment as the particle moves along the magnetic field line and then modified by the wave-particle interaction with the updated perpendicular energy, $W_{\perp n}$, given by

$$W_{\perp n} = \frac{1}{2} m_i \left(v_\perp + \Delta v_\perp\right)^2 = W_\perp + \mathrm{d}W_\perp + 2 \cdot \sqrt{W_\perp \cdot dW_\perp} \cdot \cos\theta, \tag{1}$$

where $\mathrm{d}W_\perp$ is a small increment in the perpendicular energy, $\mathrm{d}W_\perp = \frac{1}{2} m_i \left(\Delta v_\perp\right)^2$. In the present study, $\mathrm{d}W_\perp$ is chosen from a Gaussian probability distribution $F(\mathrm{d}W_\perp) = \exp\left(-\mathrm{d}W_\perp^2 / 2\sigma_i^2\right) / 2\pi\sigma_i$, where θ is a random

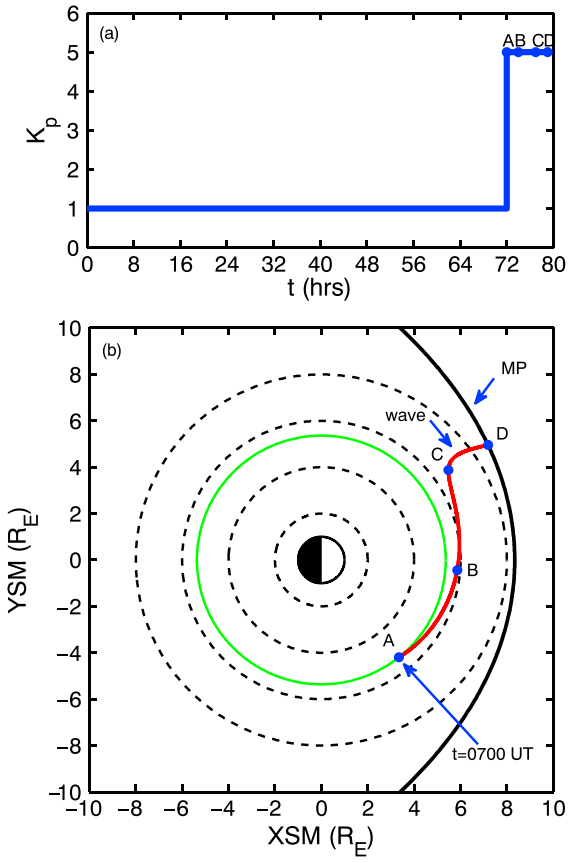

Figure 1. (a) Time variations of the assumed geomagnetic activity index *Kp*. (b) The equatorial drift trajectory of the flux tube in SM coordinates, with the Sun to the right. The black line in Figure 1b is the magnetopause determined by the model of *Shue et al.* [1998] with the southward component of the interplanetary magnetic field $B_{z\mathrm{IMF}} = -10.5$ nT and solar wind dynamics pressure $P_{sw} = 3.6$ nPa. The black dashed circles in Figure 1b are at $L = 2$, 4, 6, and 8, respectively. The flux tube corotates for 72 h under $Kp = 1$ (green solid line in Figure 1b). At t =72 h(0700 UT), as *Kp* increases to 5 in Figure 1a, the flux tube starts drifting outward from $L = 5.5$ and ends at $L = 8.73$ (red solid line in Figure 1b). The four black dots (A, B, C, and D) are located at $L = 5.5$, 5.97, 6.73, and 8.73 in Figure 1b (t = 72, 74, 77, and 79 h in Figure 1a), respectively.

angle uniformly distributed between 0 and 2π. The standard deviation σ_i is given as [*Singh and Hwang*, 1987; *Lin et al.*, 1992]

$$\sigma_i = \frac{q_i^2}{2m_i} P_i \triangle t, \tag{2}$$

where P_i is the spectral power density in the vicinity of the gyrofrequency of the ion species *i* in units of $V^2\ m^{-2}\ Hz^{-1}$. If the broadband fluctuating perpendicular electric field has a strength $\delta E_\perp$ and a bandwidth Δf, then the spectral power density is given by [*Ichimaru*, 1975]

$$P_i = \delta E_\perp^2 / \Delta f. \tag{3}$$

Details about the method of implementing the wave heating are described in *Lin et al.* [1992].

2.4. Initial Condition of Simulation

The plasmaspheric equilibrium conditions are obtained by first running the FLIP model along for the entire flux tube from 120 km in the Northern Hemisphere to 120 km in the Southern Hemisphere during an extended quiet geomagnetic activity period. Time variations of the assumed geomagnetic index *Kp* and the equatorial drift trajectory of the flux tube during the simulation are shown in Figure 1. The geomagnetic index *Kp* is set to be 1 within the first 72 h in Figure 1a and used in the McIlwain E5D electric field model to evaluate the flux tube drift trajectory in the magnetic equatorial plane for a corotating dipole flux tube. The FLIP simulation is run with the flux tube corotating with the Earth at $L = 5.5$ as shown by the green line in Figure 1b, where *L* is the McIlwain parameter [*McIlwain*, 1961] and is the equatorial distance of a field line in the Earth radius in the case of the dipole magnetic field, for 72 h of physical time. The geophysical parameters solar 10.7 cm radio flux F107 and its 81 day average F107A are set to be 140 and used in the FLIP model to determine the ionospheric conditions. At the end of the FLIP simulation, the time is 0700 UT (0632 LT and 0917 LT at the footprints of the flux tube in the Northern and Southern Hemispheres, respectively). We then remove the segment above 800 km altitude of the FLIP solution and replace it with the simulation particles of ion species O^+, H^+, and He^+ into the semikinetic domain through the Monte Carlo method [*Aldrich*, 1985] based on the ion densities, velocities, and temperatures from the FLIP simulation results along the field line, assuming drifting Maxwellian velocity distributions in the phase space.

The *Kp* index is increased from 1 to 5 approximately as a step function at point A (t = 72 h) in Figure 1a and remains constant in the following 7 h (through A to D). The flux tube starts to drift along the equatorial trajectory shown as the red line in Figure 1b in the solar magnetic (SM) coordinate system. In addition, the *z* component of the interplanetary magnetic field and the solar wind dynamic pressure are chosen as $B_{z\mathrm{IMF}} = -10.5$ nT and $P_{sw} = 3.6$ nPa, respectively, to be used to determine the location of the magnetopause in the empirical magnetopause model of *Shue et al.* [1998] as shown by the black line in Figure 1b. The flux tube contacts the dayside magnetopause at $L = 8.73$ in the afternoon quadrant after drifting 7 h from its location of $L = 5.5$ and universal time of 0700 UT through the nominal plasmaspheric plume. The points A, B, C,

and D in Figure 1b are located at $L = 5.5$, 5.97, 6.73, and 8.73, respectively. It takes about 2 h for the flux tube to travel through the trajectory between the points C and D.

The flux tube starts drift at 0924 magnetic local time (MLT) at the beginning of the event in the present simulation. The quantitative results of the simulation depend on the initial location of the flux tube, since the equatorial drift trajectories and the initial density distributions along the magnetic field line will be different due to the different starting locations of the flux tube at the beginning of the enhanced geomagnetic activity. The focus of this study is a first step toward determining the effects of plasmaspheric mass loading on the local reconnection rate near the dayside magnetopause and the effects of the wave-particle interaction. More quantitative tests will be conducted in future studies.

3. Simulation Results

3.1. Plasma Transport Without Wave-Particle Interaction

We first present simulation results of the plasma transport through the plasmaspheric plume without wave heating of the ions inside the flux tube. The influence of the wave heating on the plasma transport along the magnetic field line will be discussed in section 3.2. Before preceding to present simulation results, we emphasize that while a radially convecting dipole field line may go to different L shells, in the simulations the gyro centers of all particles moving with an "isolated" single magnetic field line and particles centered on a different field line do not come into our simulation domain. Therefore, no clipping effects are introduced in the simulations.

Since dayside magnetopause reconnection for southward interplanetary magnetic field (IMF) occurs at low latitudes, around the equator, the equatorial plasma density is a crucial parameter in measuring the reconnection rate. In Figure 2 we show the equatorial densities of O^+, H^+, and He^+ ions as a function of L shell during the flux tube drift along the segment of the trajectory shown as the red line in Figure 1. The equatorial O^+ and He^+ densities are multiplied by 10^4 and 10, respectively, in order to clearly show them in the same dynamic range as of the H^+ densities. The black dotted lines represent density variations as L^{-4}. Since the flux tube volume is proportional to L^4, the equatorial densities of the three ion species are expected to vary as the three dotted lines if there is no mass flux entering or leaving the flux tube. The equatorial H^+ and He^+ densities essentially follow the flux tube volume expansion, decreasing with L but slightly higher than the density of adiabatic expansion. The equatorial densities of H^+ and He^+ at $L = 8.73$ are greater than the expected values by about 5% and 11%, respectively, associated with the filling from the underlying ionosphere. However, equatorial O^+ densities deviate significantly from the expected values from $L = 5.97$ to $L = 8.73$. First, from points A to B, the equatorial O^+ density mostly follow the flux tube volume change in the trajectory segment between $L = 5.5$ and $L = 5.97$, decreasing as L^{-4}; second, from points B to C, the equatorial O^+ density increases rapidly between $L = 5.97$ and $L = 6.85$; and third, from points C to D, the equatorial O^+ density remains nearly constant or decreases slightly with L shell.

The equatorial O^+ density variation can be understood by examining the O^+ velocity distributions. In Figure 3 we show the O^+ (first and second rows) and H^+ (third and fourth rows) parallel velocity distributions above 800 km altitude along the flux tube at different L shells on the course of the flux tube drift toward the dayside magnetopause. The parallel velocity distributions are calculated by binning particles according to their positions and integrating the velocity distribution $f(s, v_{\parallel}, v_{\perp})$ over all the gyrospeeds, $v_{\perp}$. s is the particle's position along the magnetic field line, which is negative and positive in the Northern and Southern Hemispheres, respectively. The time interval between two neighboring panels is 1 h. Note that the length of the flux tube increases with L shell. The number of O^+ particles at 800 km in both hemispheres increases by a factor of 2, while the flux tube drifts from points A to C in Figure 1, due to two processes: (1) the solar EUV radiation increases the photoionization rates and (2) additional portions of the high-density ionosphere are "pulled out" from both hemispheres associated with the increment in the L value as the flux tube drifts poleward. During the same time period, the maximum parallel velocity and gyrospeed (data not shown) of O^+ particles at 800 km altitude in both hemispheres increase from 4 km/s to 5.9 km/s and from 5 km/s to 6.3 km/s, respectively, because of solar EUV heating of the dayside thermosphere/ionosphere. The maximum kinetic energy of O^+ ion at 800 km altitude increases from 3.42 eV to 6.22 eV. In the present study, the total potential energy is defined as the sum of the gravitational potential energy and the electric potential energy. The total potential energy difference of O^+ ions between the equator and 800 km altitude is about 5 eV. Thus, the solar EUV heating results in a fraction of O^+ particles at 800 km altitude which possess enough kinetic energy to overcome the potential barrier and reach the equator. Because of the increases in both kinetic energy and

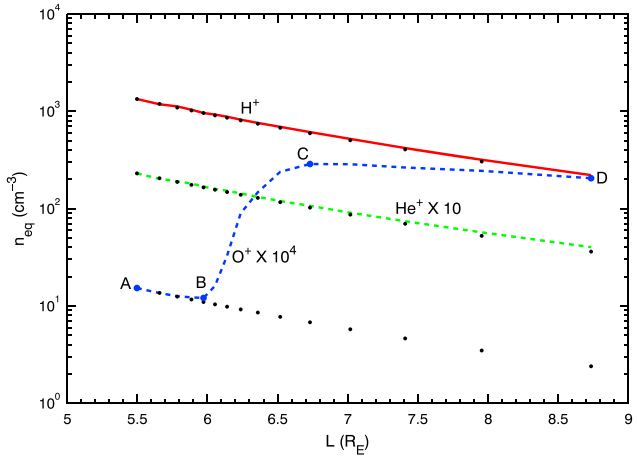

Figure 2. Variations of the equatorial densities of H^+ (red), O^+ (blue), and He^+ (green) ions with L during the drift of the flux tube along the trajectory shown in Figure 1. The equatorial densities of O^+ and He^+ are multiplied by 10^4 and 10, respectively, in order to clearly show them in the same dynamic range as of the H^+ densities. The black dotted lines represent density variation with L^{-4}.

the number density of O^+ ions at 800 km altitude together with the decrease in the number density at high altitudes caused by the flux tube volume expansion, O^+ particles move upward to fill the flux tube which is evident as the increase of the number of O^+ particles at high altitudes. The parallel velocities of upflowing O^+ ions are relatively small, and it takes time for them to arrive at the equator. Therefore, the O^+ equatorial density in Figure 2 first decreases due to the flux tube volume expansion, then increases when the upward ionospheric particles start to reach the equator and filling prevails over the effect of the volume expansion, and finally decreases slowly with L as the radial drift velocity (data not shown) is greater at large geocentric distances which results in the L shell of the drifting flux tube increases quickly and the effect of the volume expansion becomes dominant again.

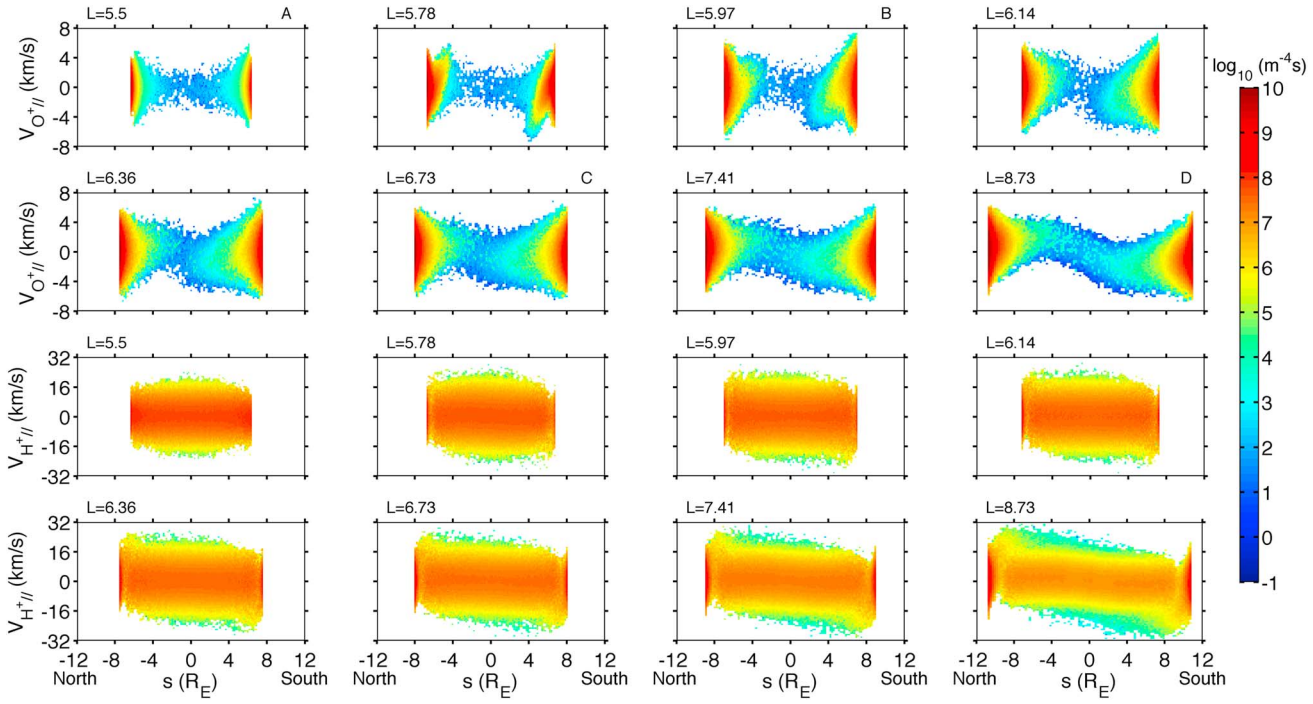

Figure 3. (first and second rows) O^+ and (third and fourth rows) H^+ parallel velocity distributions along the magnetic field line above 800 km altitude during the flux tube drift, calculated from the simulation without the wave-particle interaction. The particle position, s, is negative (positive) in the Northern (Southern) Hemisphere. The positive parallel velocity is from the Northern to the Southern Hemispheres along the magnetic field line.

The essential L^{-4} dependence of the equatorial H^+ and He^+ densities can also be more clearly illustrated by their velocity distributions. All of the H^+ and He^+ particles with the upward parallel velocity can pass the equator and move into the other hemisphere, since their total potential energies decrease from 800 km altitude to the equator. Although the number of H^+ ions at 800 km altitude in both hemispheres increases as seen in Figure 3, the number of H^+ ions at high altitudes almost remains the same during the flux tube drift. This is because the initial H^+ density distribution is close to equilibrium. The equatorial H^+ density continues decreasing, governed essentially by the expansion of the flux tube volume associated with the outward drift of the flux tube. On the other hand, the H^+ parallel bulk velocities approximately peak at $s = -8.5$ and $s = 8$ in the Northern and Southern Hemispheres, respectively, when the flux tube reaches the magnetopause at $L = 8.73$ shown in the last panel of Figure 3 (fourth row), due to the net effect of the electric field, the centrifugal force, the gravitational force, and Coulomb collisions. The number of H^+ particles is the minimum at the same locations because of the conservation of the number flux. The He^+ parallel velocity distributions (data not shown) demonstrate similar features as those of H^+ ions. The filling processes of H^+ and He^+ ions play a secondary role in the variation of their equatorial densities, compared with the effect of the flux tube volume expansion; thus, equatorial H^+ and He^+ densities decrease essentially in proportion to L^{-4} during the whole time period of the flux tube drift as shown in Figure 2. *Tu et al.* [2006] showed that the equatorial densities in both filled flux tubes and plasma trough drop with L^{-4}. However, due to the limited observations, we have not been able to find any one which demonstrated that the equatorial density in the plasmaspheric plumes varies with L^{-4}.

3.2. Effects of Wave-Particle Interaction

We now consider effects of the wave-particle interaction on the plasmaspheric ion transport to the dayside magnetopause through the plasmaspheric plume. As discussed before, a parameterized method is used to simulate the perpendicular wave heating by broadband EMIC waves. The broadband EMIC waves have been observed in a large range of L shells from $L = 3$ to $L = 10$ [e.g., *Anderson et al.*, 1992; *Usanova et al.*, 2013; *Meredith et al.*, 2014]. EMIC waves can be generated by anisotropic ($T_\perp > T_\parallel$) ring current ions in the inner magnetosphere during storms and substorms [*Jordanova et al.*, 2001] or associated with solar wind pressure fluctuations in the outer dayside magnetosphere [e.g., *Arnoldy et al.*, 2005]. *Anderson et al.* [1992] studied the occurrence of EMIC waves in the equatorial magnetosphere from $L = 3.5$ to $L = 9$ at all local times, using Active Magnetospheric Particle Tracer Explorers (AMPTE)/CCE data and found that EMIC waves occurred most frequently in the region $L > 7$ in the early afternoon (magnetic local time (MLT) of 1200–1500 MLT). *Usanova et al.* [2013] found that the L shell/MLT distribution of EMIC waves in plasmaspheric plumes peaked at MLT = 12–16 beyond the geosynchronous orbit from the Cluster observations. Thus, in the present study we incorporate the effects of the perpendicular ion heating by broadband EMIC waves on three ion species (O^+, H^+, and He^+) from $L = 6.73$ to $L = 8.73$ as the flux tube follows the trajectory between points C and D in Figure 1b, which lies around 1420 MLT.

In view of the limited knowledge regarding the wave power levels and the wave latitudinal distribution, the electric power spectral level (P_i in equation (2)) of EMIC waves in the vicinity of the H^+ ion cyclotron frequency is assumed to be $P_{H^+} = P_0 \cos^8 \lambda \exp\left(-W^2_{H^+\perp}/50^2\right)$ V^2 m^{-2} Hz^{-1} [*Lin et al.*, 1992], where λ is the magnetic latitude. The wave power is peaked at the equator and significant up to ±40° latitude. The factor $\exp\left(-W^2_{H^+\perp}/50^2\right)$ is included in order to make the wave power decrease rapidly when the particle perpendicular energy is above 50 eV ($W_{H^+\perp}$ in units of eV), which is assumed to be the saturation of ion energy gain and corresponds to the H^+ gyrospeed 98 km/s. *Lin et al.* [1992] considered that the electric field power levels of EMIC waves near the H^+ ion gyrofrequency ranged from 10^{-14} to 10^{-9} V^2 m^{-2} Hz^{-1}. Three different equatorial nominal power levels $P_0 = 10^{-9}$, 10^{-10}, and 10^{-11} V^2 m^{-2} Hz^{-1} are applied in the present simulations. The electric field power levels of broadband EMIC waves are assumed to vary as $\omega^{-2.2}$, where ω is the wave frequency [*Chang et al.*, 1986]. Thus, the relationships among the wave power levels at the gyrofrequencies of O^+, H^+, and He^+ ions are $P_{He^+} = \left(m_{He^+}/m_{H^+}\right)^{2.2} P_{H^+}$ and $P_{O^+} = \left(m_{O^+}/m_{H^+}\right)^{2.2} P_{H^+}$. The O^+, H^+, and He^+ ions are heated by broadband EMIC waves, in the region extending over a significant portion of the geomagnetic field line around the equator.

To demonstrate the effects of the perpendicular wave heating, we display in Figure 4 the density distributions of O^+, H^+, and He^+ ions and the total mass density distributions along the magnetic field line, as the flux tube reaches the dayside magnetopause. The black, green, blue, and red lines are the results from simulations without the wave heating ($P_0 = 0$), with the wave heating for about 2 h including a weak wave power level

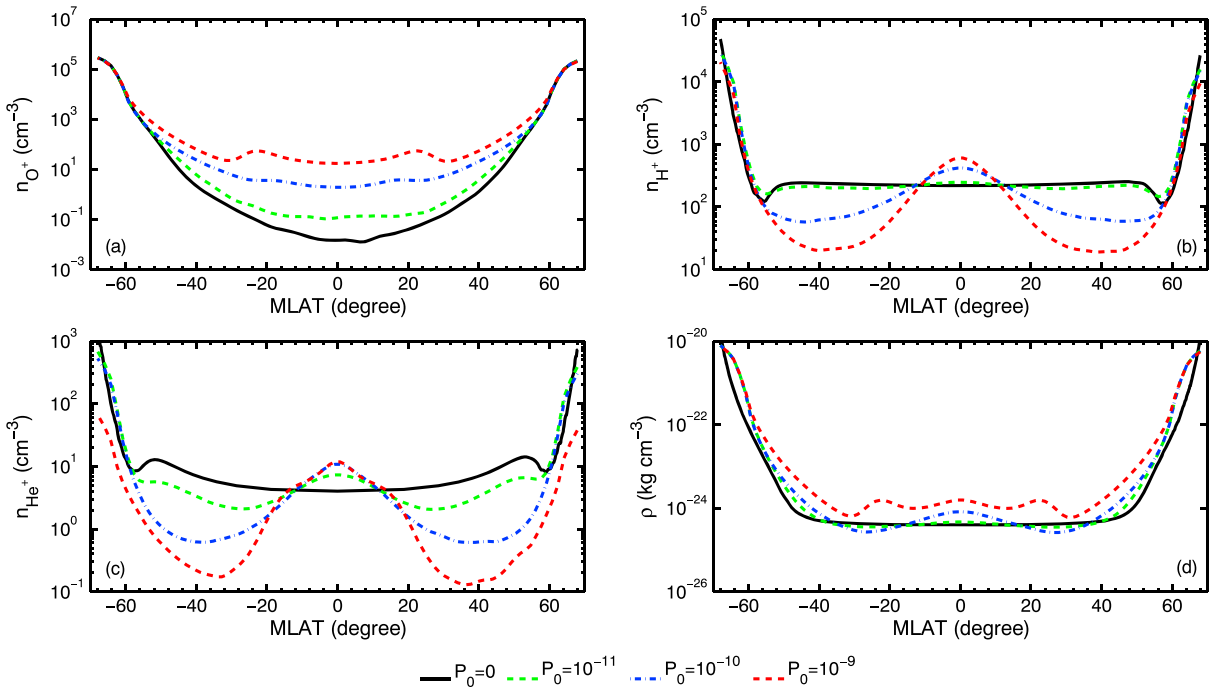

Figure 4. (a) O^+, (b) H^+, (c) He^+ number densities, and (d) the total mass density as a function of the magnetic latitude when the flux tube reaches the dayside magnetopause at $L = 8.73$. The results come from the simulations without the wave heating ($P_0 = 0$, black lines), with a weak wave power level ($P_0 = 10^{-11}$ V^2 m^{-2} Hz^{-1}, green lines), a medium wave power level ($P_0 = 10^{-10}$, blue lines), and a strong wave power level ($P_0 = 10^{-9}$ V^2 m^{-2} Hz^{-1}, red lines), respectively.

($P_0 = 10^{-11}$ V^2 m^{-2} Hz^{-1}), a medium wave power level ($P_0 = 10^{-10}$ V^2 m^{-2} Hz^{-1}), and a strong wave power level ($P_0 = 10^{-9}$ V^2 m^{-2} Hz^{-1}), respectively, when the flux tube traverses from $L = 6.73$ to the magnetopause at $L = 8.73$. Note that the foot of the field line is in the ionosphere where the density is high (up to 10^5 cm^{-3}), although the assumed dipole field line reaches the magnetopause at the equator. It is clear from Figure 4 that the equatorial densities of all three ion species increase under the influence of the wave heating. For example, the O^+ equatorial density in the case with $P_0 = 10^{-9}$ V^2 m^{-2} Hz^{-1} is about 3 orders of magnitude larger than that from the simulation without the wave heating as shown in Figure 4a. The H^+ and He^+ densities are peaked at the equator (see Figures 4b and 4c), while the O^+ densities are peaked at the magnetic latitude of ±22° with a density minimum at the equator when $P_0 = 10^{-9}$ V^2 m^{-2} Hz^{-1}.

In order to gain insight to the density distributions of the O^+, He^+, and H^+ ions, we again examine the velocity distributions of these ions. Figure 5 displays the parallel velocity and gyrospeed distributions of H^+, He^+, and O^+ ions above 800 km when the flux tube reaches the dayside magnetopause. The top and second rows in Figure 5 come from the simulation results including the wave heating with $P_0 = 10^{-11}$ V^2 m^{-2} Hz^{-1} for 2 h. Figure 5 (bottom row) is the simulation results in section 3.1 without the wave-particle interaction. The overall perpendicular energies of the three ion species increase due to the wave heating as shown by comparing Figure 5 (second and third rows), even though the individual ion either lose or gain perpendicular energy at each time step because of the stochastic heating process. The parallel velocities in Figure 5 (top row) increase associated with the perpendicular energy, since the magnetic mirror force converts the perpendicular energy to the parallel energy as the particles move upward along the field line. An almost isolated peak appears around the equator in the He^+ velocity distributions due to the perpendicular energization processes, agreeing with the density distributions with a bump around the equator as shown in Figure 4c (green dashed lines). With the increasing wave power, more He^+ ions are trapped around the equator at the cost of decreasing number of particles at lower latitudes (around ±40°). H^+ density distribution displays similar equatorial bumps when the wave power is above $P_0 = 10^{-10}$ V^2 m^{-2} Hz^{-1}.

The effects of the wave-particle interaction on trapping different ion species around the equator can be more clearly illustrated with the ion pitch angle distributions. As an example, Figure 6 shows the He^+ pitch angle distributions as a function of particle position when the flux tube reaches the dayside magnetopause. The results

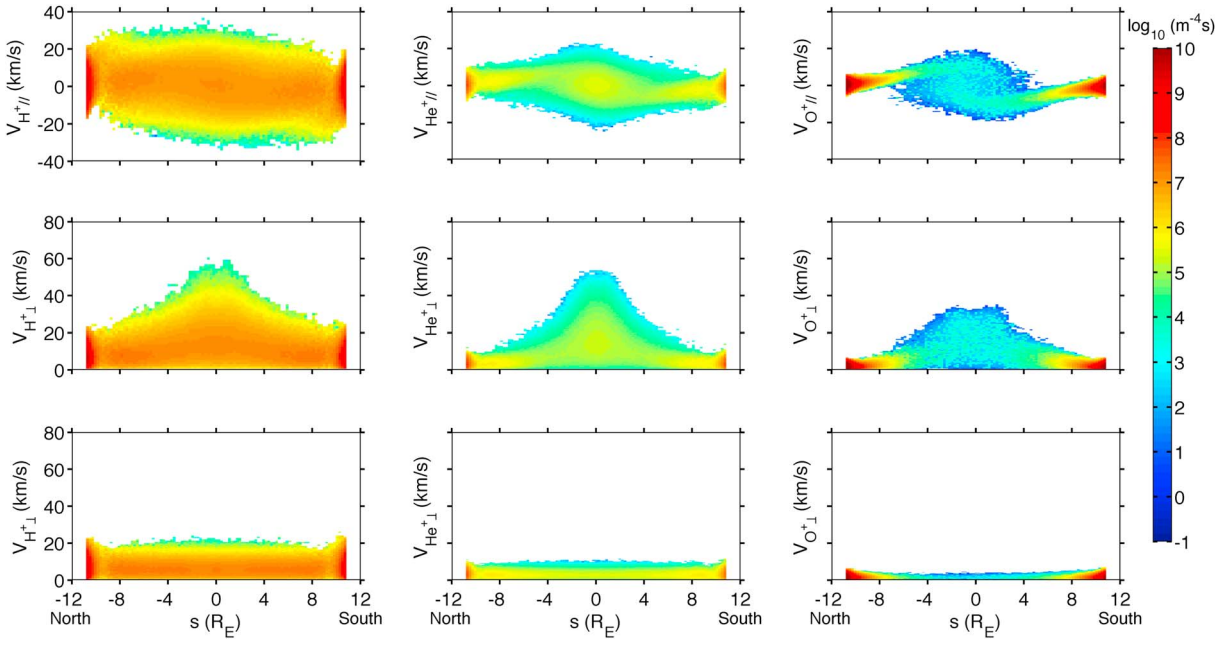

Figure 5. (top row) Parallel velocity and (middle row) gyrospeed distributions of H^+, He^+, and O^+ ions when the flux tube contacts the dayside magnetopause with the wave power of $P_0 = 10^{-11}$ V^2 m^{-2} Hz^{-1}. (bottom row) Gyrospeed distributions of H^+, He^+, and O^+ ions at the dayside magnetopause without the wave-particle interaction during the simulation.

are from simulations without the wave-particle interaction and with the wave-particle interaction under different wave power levels. The pitch angle distribution is evaluated by binning the particles according to their positions and their pitch angles per volume. The 0° pitch angle represents the particles without the perpendicular energy streaming from the Northern Hemisphere to the Southern Hemisphere along the magnetic field line. All of the particle's energy is converted to the perpendicular energy when the pitch angle is equal to 90°. Comparing the four panels in Figure 6, we find that (1) the mirror points of particles move gradually toward the equator as the particles bounce back and forth in the region of the wave-particle interaction; (2) more particles with pitch angles in the vicinity of 90° appear at the equator when the wave perpendicular heating process is included; and (3) the increase in the nominal wave power level from $P_0 = 10^{-11}$ to 10^{-9} V^2 m^{-2} Hz^{-1} leads to stronger effects on trapping He^+ ions close to the equator.

H^+ pitch angle distributions (data not shown) exhibit similar features as those of He^+ ions in Figure 6, except that the effects of the wave-particle interaction on trapping ions at the equator are weaker for H^+ ions. Since the electric power level (P_i in equation (2)) varies as $m_i^{2.2}$ and the increment in the ion perpendicular energy ($dW_{i\perp}$) is proportional to the standard deviation (σ_i in equation (2)), the increase in the gyrospeed is proportional to $m_i^{0.1}$, that is $dv_{He^+\perp} = \left(m_{He^+}/m_{H^+}\right)^{0.1} dv_{H^+\perp} = 1.15dv_{H^+\perp}$. The assumed electric power spectral levels result in smaller increments in the gyrospeeds of H^+ ions than in He^+ ions, and thus, H^+ ions need to bounce between the mirror points more times (while experiencing the wave heating) in order to be trapped at the equator. The numbers of H^+ and He^+ ions trapped around the equator increase due to the wave perpendicular heating, causing the formation of the equatorial bumps in the H^+ and He^+ density distributions in Figures 4b and 4c.

The pitch angle distributions of O^+ ions shown in Figure 7, however, are substantially different from those of He^+ and H^+ ions. Similar to the H^+ and He^+ ions, more O^+ particles move upward to high altitudes under the wave perpendicular energization as seen by comparing the other panels with the first panel. While comparing Figure 7 (top left) with that in Figure 6, we find that the O^+ distribution without the wave-particle interaction is more field aligned than that of He^+ ions. Therefore, most O^+ particles need to experience the wave heating for longer time period than He^+ particles in order to be trapped at the equator with 90° pitch angle. After 2 h of the wave-particle interaction with $P_0 = 10^{-9}$ V^2 m^{-2} Hz^{-1}, the O^+ particles at high altitudes bounce between $s = \pm 4$ (latitude about ±22°) around the equator (see Figure 7, bottom right). The ratio of the magnetic field strength between $s = 4$ (or $s = -4$) and $s = 0$ is about 1.9. For the particle having mirror points at $s = \pm 4$, its pitch angle at the equator is about 43.5° or 136.5° if its magnetic moment is conserved.

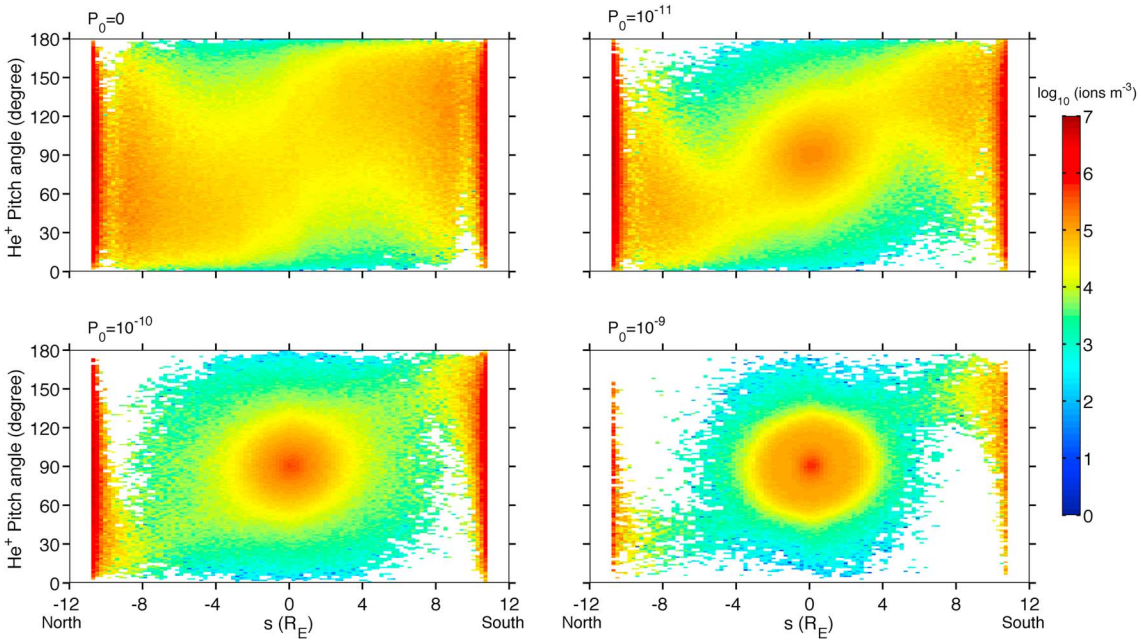

Figure 6. The He^+ pitch angle distributions when the flux tube contacts the dayside magnetopause. The results are from simulations with the wave power $P_0 = 0$, $P_0 = 10^{-11}$, 10^{-10}, and 10^{-9} V^2 m^{-2} Hz^{-1}, respectively.

The two void regions off the equator with the pitch angle range of about 70° to 110° in Figure 7 (bottom right) can be understood by examining the parallel electric field distribution along the magnetic field line. The field-aligned electric fields as a function of magnetic latitude at high altitudes after 1 h of the wave-particle interaction with different wave power levels are shown in Figure 8, in which the positive value is from the Northern Hemisphere to the Southern Hemisphere. The field-aligned electric field [see *Wang et al.*, 2015, equation (6)] is primarily determined by the electron pressure gradient. The electric field is directed downward from the equator at high altitudes when $P_0 > 10^{-10}$ V^2 m^{-2} Hz^{-1} associated with downward electron pressure gradients, and the stronger wave power level leads to a larger amplitude of the downward

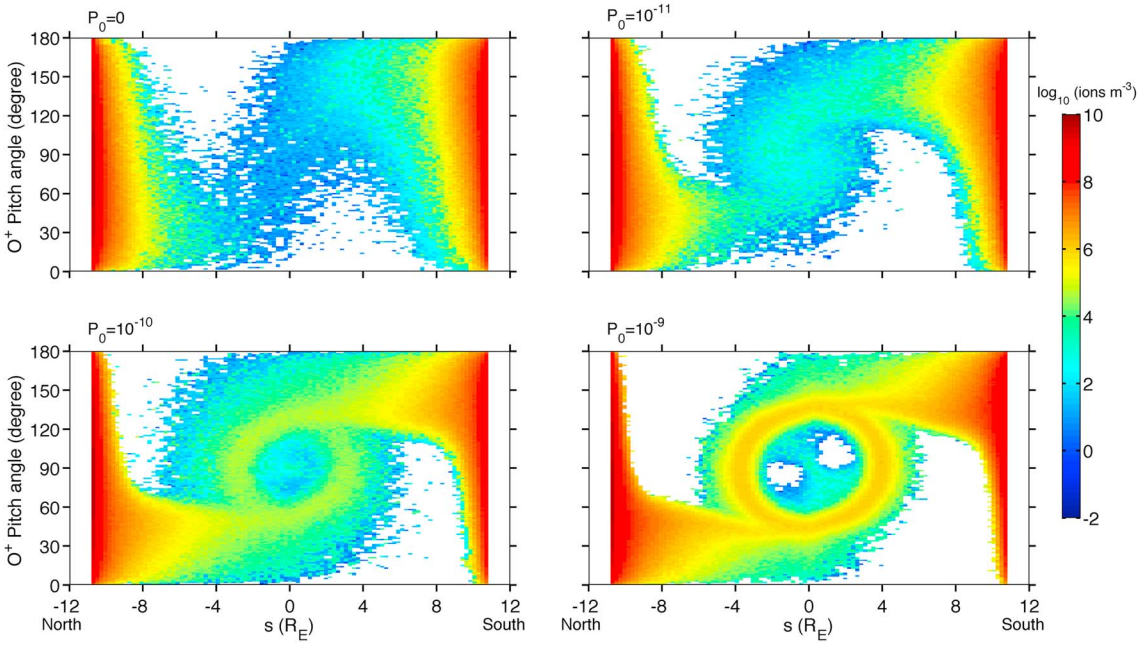

Figure 7. Same format as Figure 6 but for O^+ ions.

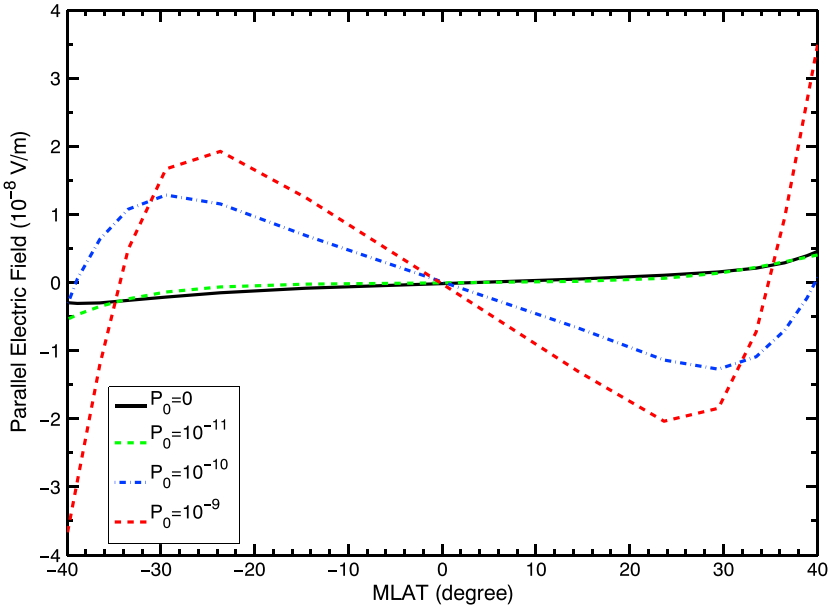

Figure 8. The parallel electric fields as a function of magnetic latitude from the simulations with the wave power $P_0 = 0$, $P_0 = 10^{-11}$, 10^{-10}, and 10^{-9} V^2 m^{-2} Hz^{-1}, respectively.

electric field. The downward electric field may reflect some O^+ ions with small kinetic energies which are previously trapped near the equator to lower altitudes. For example, the downward electric field force is greater than the upward magnetic mirror force for O^+ particles with kinetic energy less than 1 eV and pitch angle close to 90° at $s = 4$ when $P_0 = 10^{-9}$ V^2 m^{-2} Hz^{-1}. Therefore, these O^+ particles are pushed to move downward, resulting in the two void regions off the equator with the pitch angle range of about 70° to 110° . Note that the electric field around the equator is near zero, and thus, there are some O^+ particles remain in that region. The electric field and the magnetic mirror force together trap the O^+ to bounce back and forth between $s = \pm 4$, and thus, two density peaks appear in the Northern and Southern Hemispheres, respectively, shown in Figure 4a when $P_0 = 10^{-9}$ V^2 m^{-2} Hz^{-1}. The influence of the downward electric field is strongest for O^+ ions, since the kinetic energy of O^+ ions at high altitudes is smallest after overcoming gravity due to the heavy O^+ ion mass compared to those of lighter H^+ and He^+.

3.3. Possible Impacts on the Dayside Magnetopause Reconnection

The cold and dense plasmaspheric plasma transported to the dayside magnetopause through the plasmaspheric plume may have significant impacts on dayside magnetopause reconnection. Table 1 shows that the total mass density within the plasmaspheric plume at the magnetopause may be up to 3 orders of magnitude higher than the nominal mass density in the surrounding region. Note that the mass density distributions within the plasmaspheric plume are calculated from the simulated O^+, H^+, and He^+ number density distributions. The mass loading of the dense plasmaspheric ions at the dayside magnetopause will influence the reconnection process by lowering the hybrid Alfvén speed (V_A) significantly and thus the dimensionless reconnection rate. The hybrid Alfvén speed, which takes into account the asymmetric densities and magnetic field intensities in the magnetosheath and magnetosphere, is given as [*Cassak and Shay*, 2007]

$$V_A = \sqrt{\frac{B_m B_s \left(B_m + B_s\right)}{\mu_0 \left(\rho_m B_s + \rho_s B_m\right)}}, \tag{4}$$

where subscripts m and s denote the parameters in the magnetosphere and magnetosheath, respectively, B is the magnetic field intensity, μ_0 is the free space magnetic permeability, and ρ is the mass density. The intensity of the magnetic field in the magnetosheath is assumed to be 4 times as the strength of the interplanetary magnetic field in the high Mache number case, then $B_s \approx 4B_{IMF} \approx 42$ nT. The strength of the magnetospheric dipole magnetic field in the equatorial plane at $L = 8.73$ is $B_m = 46.7$ nT. The number densities of the plasma in the magnetosheath and in the plasma trough without plumes are assumed to be 10 cm^{-3} and 0.25 cm^{-3}, respectively, in which the ions are assumed to consist of H^+. The equatorial magnetospheric mass

Table 1. Comparisons of Hybrid Alfvén Speeds[a]

Equatorial Nominal Power Level P_0 ($V^2\ m^{-2}\ Hz^{-1}$)	Equatorial Mass Density (amu/cm^3)	Hybrid Alfvén Speed (km/s)
no mass loading	0.25	417
0	237	89
10^{-11}	280	82
10^{-10}	492	63
10^{-9}	935	46

[a]Assuming $B_m = 46.7$ nT, $B_s = 42$ nT, and $\rho_s = 10$ amu/cm^3.

densities and hybrid Alfvén speeds (equation (4)) at the magnetopause with/without plasmaspheric mass loading under different wave power levels are listed in Table 1. The reconnection jet velocities were 362 km/s for an nonplume event and 162 km/s for the plume event, respectively, measured near simultaneously by two Time History of Events and Macroscale Interactions (THEMIS) spacecraft at the dayside magnetopause [*Walsh et al.*, 2014a]. They are comparable with the results of the first two cases in Table 1.

The dimensionless reconnection rate is proportional to the Alfvén speed [*Birn and Hesse*, 2007; *Cassak and Shay*, 2007]; thus, smaller Alfvén speeds result in decreased reconnection rates. As listed in Table 1, the hybrid Alfvén speeds in the presence of the dense plasmaspheric ions without the wave-particle interaction ($P_0 = 0$) and under strong wave perpendicular heating for 2 h ($P_0 = 10^{-9}\ V^2\ m^{-2}\ Hz^{-1}$) are 21% and 11% of the one in the absence of the plasmaspheric ions. The local reconnection rate drops significantly at the location where the dense plasmaspheric ions load at the dayside magnetopause and the local reconnection rate may decrease by 90% when including the effects of the wave-particle interaction. The stronger wave power level, the smaller reconnection rate. On the other hand, if the ion particles interact with waves for longer time, the local Alfvén speed and the reconnection rate may be even smaller. For example, when the flux tube at $L = 5.5$ with the same initial conditions follows the drift trajectory shown in Figure 1 and effects of the wave-particle interaction are included for 4 h (from $6.14 \le L \le 8.73$) with a medium wave power of $P_0 = 10^{-10}\ V^2\ m^{-2}\ Hz^{-1}$, the O^+ density distribution at $L = 8.73$ is similar to that corresponding to the case with a strong wave power of $P_0 = 10^{-9}\ V^2\ m^{-2}\ Hz^{-1}$ in Figure 4a and the equatorial mass density at $L = 8.73$ is larger than that from the simulation with $P_0 = 10^{-10}\ V^2\ m^{-2}\ Hz^{-1}$ for 2 h, resulting in a smaller local Alfvén speed (56 km/s) and thus a smaller local reconnection rate.

In the above we have used our simulation to estimate the effect of the plasmaspheric plume on magnetopause reconnection. An important assumption made in this assessment is the dipole of magnetospheric field. Here we discuss the possible consequences of this assumption. First, it has been noted that the magnetospheric field could be substantially different from a dipole field in particular when the magnetosphere is highly compressed. It has been shown that the magnetic field could have a local maximum at the subsolar magnetopause [e.g., *Mead*, 1964]. Following this fact, argument has been made that the magnetic field is weaker near the magnetopause in higher latitudes. If a magnetic field line starting at the subsolar is along the magnetopause and then turns in the cusp region toward the ionosphere, there is a magnetic cavity in the cusp region. Particles can be trapped between the two mirror points at the subsolar magnetopause and the ionosphere. These trapped particles would form an additional population to the four populations identified by *Wang et al.* [2015]. However, there is a question whether the subsolar magnetopause field line does go along the magnetopause to the high latitudes or not. A magnetic field line goes along the dayside magnetopause if this portion of the magnetopause is closed, i.e., there is no reconnection taking place in this region, or in large scales the magnetopause is a tangential discontinuity. It is commonly accepted that the dayside magnetopause is closed [e.g., *Song and Russell*, 1992] for northward IMF. This magnetic cavity may indeed exist for northward IMF. However, for southward IMF, it is commonly believed that reconnection takes place in the low-latitude magnetopause and magnetospheric field in the dayside magnetopause is open, as shown in Figure 9. In the case we have simulated, the plasmaspheric plume is formed associated with a strongly enhanced sunward convection which can be produced only under strongly southward IMF conditions. Therefore, under this condition, although the subsolar magnetopause has a magnetic field maximum, it is still the weakest point along the magnetic field line and the trapping due to the subsolar magnetopause field will not occur. Our simulation qualitatively represents correctly the physical processes associated with

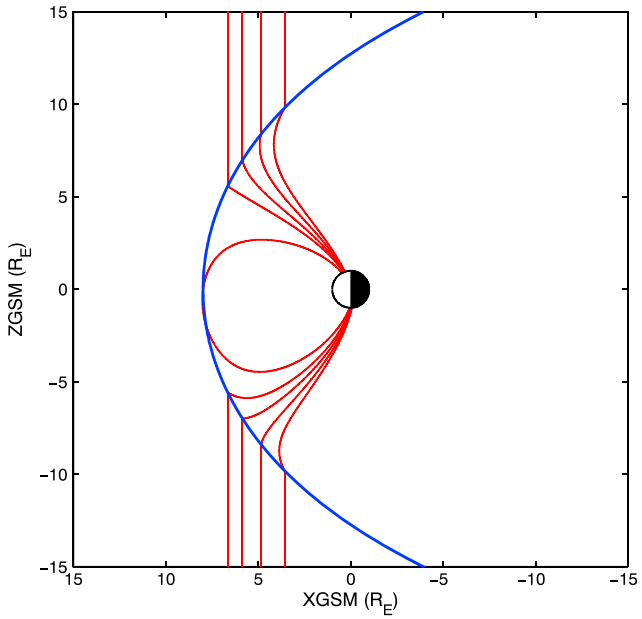

Figure 9. Schematic illustration of the geometry of the magnetopause and the magnetic field lines on dayside in the meridional plane with the Sun to the left. The blue line and red lines are the magnetopause and magnetic field lines, respectively.

the particle motion. Here we further recall that *Wang et al.* [2015] have shown that there is a trapped population between the equator and the ionosphere. However, the trapping is due to the gravity and we believe that the gravity trapping remains dominant to any perceived possible trapping due to compression of the dayside magnetopause.

Nevertheless, the last-closed field line at the subsolar magnetopause is stronger than the dipole magnetic field in strength. In principle, there is a doubling effect generically occurring at the magnetopause associated with the shielding effect of the magnetopause current, i.e., $B_{mp} \sim 2B_{\text{dipole}}$. However, the reconnection effect tends to reduce the factor. The empirical *Tsyganenko* model [*Tsyganenko et al.*, 1999] has indicated this field enhancement is about a factor of 1.2 ~ 1.3. With this increase in the field strength, for particles coming from the ionosphere their equatorial pitch angles will be increased by about 0.2°. The equatorial densities may be, depending on the flux tube geometry, 20% ~ 30% larger than those in the dipole field with the same magnetic flux. Then the equatorial Alfvén speed is enhanced by 9.5% ~ 14% and the net effect of the plasmaspheric plume on the reconnection rate would be a decrease of about 80%, remaining to be substantial.

On the other hand, the drift trajectory of the flux tube is calculated by using a static dipole magnetic model and *E5D* convection model in the present paper, which is different from the realistic drift path. The different drift trajectories may result in different final results. We are further exploring whether our plasmaspheric formalism can be extended to the outer magnetosphere and not pursuing realistic field at this stage. Although the dipolar magnetic field in the simulation model may not be the best approximation at large *L* shells, particularly under disturbed geomagnetic conditions, it does not affect qualitatively the basic conclusion. More accurate magnetic field model will be incorporated within the DyFK model in our future studies. In addition, the DyFK model is capable of providing 3-D descriptions of the plasmaspheric plume with multiple flux tubes in the outer plasmasphere simultaneously drifting toward the dayside magnetopause during periods of enhanced magnetospheric convection.

4. Summary and Discussion

In the present study, we have used the Dynamic Fluid-Kinetic (DyFK) model to simulate the transport of the plasmaspheric ions to the dayside magnetopause through the plasmaspheric plume under disturbed geomagnetic conditions. The field-aligned density distributions of O^+, H^+, and He^+ ions provide quantitative assessments of the mass loading of the plasmaspheric plasma at the dayside magnetopause, which is crucial to understanding the effects of the high-density plasmaspheric plasma on dayside magnetic reconnection

and solar wind-magnetosphere coupling. The local hybrid Alfvén speed in the presence of the dense plasmaspheric ions at the magnetopause is much lower than that in the absence of the plume, indicating a smaller local reconnection rate due to the mass loading of the plasamspheric ions through the drainage plumes under enhanced magnetospheric convection. Effects of the wave-particle interaction on the plasma density distribution along the magnetic field line in the plasmaspheric plume are also studied which further increase the equatorial density and hence reduce the reconnection rate. The kinetic features of multiple ion species (O^+, H^+, and He^+) show that O^+ ions behave differently from H^+ and He^+ ions due to the heavy O^+ ion mass under the assumed wave power levels and wave latitudinal distributions.

The plasma density at the equator in the present simulation without the wave-particle interaction is 224 cm^{-3}, about 3 orders of magnitude larger than the typical magnetospheric density (in the order of ~ 0.1 cm^{-3}), when the plasmaspheric flux tube reaches the dayside magnetopause. *Walsh et al.* [2013] conducted a statistical study of the cold high-density plasma from the plasmasphere at the dayside magnetopause based on the observations from the THEMIS spacecraft. The plume densities at the magnetopause in *Walsh et al.* [2013] can be as large as 300 cm^{-3}. The present simulations without and with low wave power provide the similar equatorial density at the magnetopause.

The plasmasphere is highly dynamic and the flux tubes in the outer plasmasphere seldom reach saturation levels due to the time-varying geomagnetic conditions. Whether the plasmaspheric plume can convect all the way to the dayside magnetopause depends on whether the time period of enhanced magnetospheric convection is sufficiently long. Therefore, how much mass can be loaded at the dayside magnetopause through the plasmaspheric plume is related to the initial density conditions of the flux tube and the period of strong geomagnetic activities, the level and spatial span of the wave-particle interaction. The DyFK model provides a useful tool to simulate evolution of the plasmaspheric plume if realistic geophysical and geomagnetic parameters, as well as the distribution and strength of the EMIC waves, are used.

The density bumps of H^+ and He^+ ions form at the equator after 2 h of the wave perpendicular heating in the present simulation. Although an H^+ density bump also appeared at the equator within 4 h of refilling including the wave-particle interaction of an initially depleted $L = 4$ flux tube in the simulation of *Lin et al.* [1992], the equatorial H^+ density was depleted during the following hours. Field-aligned electric fields directed away from the equator were developed after 4 h of refilling in *Lin et al.* [1992]. The potential drop associated with the electric field was large enough to reflect the incoming ions and expel a fraction of the previously trapped ions from the equator, resulting in the depletion of the equatorial density later on [*Lin et al.*, 1992]. If EMIC waves interact with the particles for longer time period or the wave power levels are even larger in the DyFK simulations, the intense perpendicular heating may also produce a large enough electric potential drop which may cause the H^+ density depletion at the equator. Nevertheless, we should point out that radio wave sounding of the plasmaspheric densities has not reported enhanced plasma density at the equator [*Reinisch et al.*, 2001; *Ozhogin et al.*, 2014]. More comprehensive information about the power spectral density and latitudinal distribution of broadband EMIC waves as a function of geomagnetic activity is needed to better assess the role of the wave-particle interaction in affecting the plasma transport along the magnetic field line. Different spatial locations of EMIC waves, wave power levels, and time periods during which the particles interact with waves will result in different density distributions, which will be studied in future works.

Acknowledgments
The work at UML was supported by NSF grants AGS-1303596 and 1248242 and NASA grant NNX12AD22G. All data in the paper can be obtained from Yan Wang (e-mail: Yan_Wang@student.uml.edu).

References

Aldrich, C. (1985), Particle code simulations with injected particles, *Space Sci. Rev.*, *42*(1–2), 131–144, doi:10.1007/BF00218228.

Anderson, B. J., R. E. Erlandson, and L. J. Zanetti (1992), A statistical study of Pc 1-2 magnetic pulsations in the equatorial magnetosphere: 1. Equatorial occurrence distributions, *J. Geophys. Res.*, *97*(A3), 3075–3088, doi:10.1029/91JA02706.

Arnoldy, R. L., et al. (2005), Pc 1 waves and associated unstable distributions of magnetospheric protons observed during a solar wind pressure pulse, *J. Geophys. Res.*, *110*, A07229, doi:10.1029/2005JA011041.

Birn, J., and M. Hesse (2007), Reconnection rates in driven magnetic reconnection, *Phys. Plasmas*, *14*(3), 82306, doi:10.1063/1.2752510.

Borovsky, J. E., and M. H. Denton (2006), Effect of plasmaspheric drainage plumes on solar-wind/magnetosphere coupling, *Geophys. Res. Lett.*, *33*, L20101, doi:10.1029/2006GL026519.

Borovsky, J. E., and M. H. Denton (2008), A statistical look at plasmaspheric drainage plumes, *J. Geophys. Res.*, *113*, A09221, doi:10.1029/2007JA012994.

Borovsky, J. E., M. Hesse, J. Birn, and M. M. Kuznetsova (2008), What determines the reconnection rate at the dayside magnetosphere?, *J. Geophys. Res.*, *113*, A07210, doi:10.1029/2007JA012645.

Cassak, P. A., and M. A. Shay (2007), Scaling of asymmetric magnetic reconnection: General theory and collisional simulations, *Phys. Plasmas*, *14*, 102144, doi:10.1063/1.2795630.

Chang, T., G. B. Crew, N. Hershkowitz, J. R. Jasperse, J. M. Retterer, and J. D. Winningham (1986), Transverse acceleration of oxygen ions by electromagnetic ion cyclotron resonance with broad band left-hand polarized waves, *Geophys. Res. Lett.*, *13*(7), 636–639, doi:10.1029/GL013i007p00636.

Chen, A. J., and R. A. Wolf (1972), Effects on the plasmasphere of a time varying convection electric field, *Planet. Space Sci.*, *20*(4), 483–509, doi:10.1016/0032-0633(72)90080-3.

Darrouzet, F., J. De Keyser, P. M. E. Décréau, F. El Lemdani-Mazouz, and X. Valliéres (2008), Statistical analysis of plasmaspheric plumes with Cluster/WHISPER observations, *Ann. Geophys.*, *26*, 2403–2417, doi:10.5194/angeo-26-2403-2008.

Darrouzet, F., et al. (2009), Plasmaspheric density structures and dynamics: Properties observed by the CLUSTER and IMAGE missions, *Space Sci.Rev.*, *145*(1–2), 55–106, doi:10.1007/s11214-008-9438-9.

Elphic, R. C., L. A. Weiss, M. F. Thomsen, D. J. McComas, and M. B. Moldwin (1996), Evolution of plasmaspheric ions at geosynchronous orbit during times of high geomagnetic activity, *Geophys. Res. Lett.*, *23*(16), 2189–2192, doi:10.1029/96GL02085.

Fraser, B. J., J. L. Horwitz, J. A. Slavin, Z. C. Dent, and I. R. Mann (2005), Heavy ion mass loading of the geomagnetic field near the plasmapause and ULF wave implications, *Geophys. Res. Lett.*, *32*, L04102, doi:10.1029/2004GL021315.

Grebowsky, J. M. (1970), Model study of plasmapause motion, *J. Geophys. Res.*, *75*(22), 4329–4333, doi:10.1029/JA075i022p04329.

Goldstein, J., B. R. Sandel, W. T. Forrester, M. F. Thomsen, and M. R. Hairston (2005), Global plasmasphere evolution 22–23 April 2001, *J. Geophys. Res.*, *110*, A12218, doi:10.1029/2005JA011282.

Huba, J. D., G. Joyce, and J. A. Fedder (2000), Sami2 is Another Model of the Ionosphere (SAMI2): A new low-latitude ionosphere model, *J. Geophys. Res.*, *105*(A10), 23,035–23,053, doi:10.1029/2000JA000035.

Ichimaru, S. (1975), Theory of plasma heating by fluctuating electric fields-effects of correlation times, *J. Phys. Soc. Jpn.*, *39*(5), 1373–1378, doi:10.1143/JPSJ.39.1373.

Jordanova, V. K., C. J. Farrugia, R. M. Thorne, G. V. Khazanov, G. D. Reeves, and M. F. Thomsen (2001), Modeling ring current proton precipitation by electromagnetic ion cyclotron waves during the May 14–16, 1997, storm, *J. Geophys. Res.*, *106*(A1), 7–22, doi:10.1029/2000JA002008.

Lambour, R. L., L. A. Weiss, R. C. Elphic, and M. F. Thomsen (1997), Global modeling of the plasmasphere following storm sudden commencements, *J. Geophys. Res.*, *102*(A11), 24351–24368, doi:10.1029/97JA02037.

Lee, S. H., H. Zhang, Q.-G. Zong, A. Otto, H. Rème, and E. Liebert (2016), A statistical study of plasmaspheric plumes and ionospheric outflows observed at the dayside magnetopause, *J. Geophys. Res. Space Physics*, *121*, 492–506, doi:10.1002/2015JA021540.

Liemohn, M. W., G. V. Khazanov, T. E. Moore, and S. M. Guiter (1997), Self-consistent superthermal electron effects on plasmaspheric refilling, *J. Geophys. Res.*, *102*(A4), 7523–7536, doi:10.1029/96JA03962.

Lin, J., J. L. Horwitz, G. R. Wilson, C. W. Ho, and D. G. Brown (1992), A semikinetic model for early stage plasmasphere refilling: 2. Effects of wave-particle interactions, *J. Geophys. Res.*, *97*(A2), 1121–1134, doi:10.1029/91JA02729.

McFadden, J. P., C. W. Carlson, D. Larson, J. Bonnell, F. S. Mozer, V. Angelopoulos, K.-H. Glassmeier, and U. Auster (2008), Structure of plasmaspheric plumes and their participation in magnetopause reconnection: First results from THEMIS, *Geophys. Res. Lett.*, *35*, L17S10, doi:10.1029/20008GL033677.

McIlwain, C. E. (1961), Coordinates for mapping the distribution of magnetically trapped particles, *J. Geophys. Res.*, *66*(11), 3681–3691, doi:10.1029/JZ066i011p03681.

McIlwain, C. (1986), A *Kp* dependent equatorial electric field model, *Adv. Space Res.*, *6*(3), 187–197, doi:10.1016/0273-1177(86)90331-5.

Mead, G. D. (1964), Deformation of the geomagnetic field by the solar wind, *J. Geophys. Res.*, *69*(7), 1181–1195, doi:10.1029/JZ069i007p01181.

Meredith, N. P., R. B. Horne, T. Kersten, B. J. Fraser, and R. S. Grew (2014), Global morphology and spectral properties of EMIC waves derived from CRRES observations, *J. Geophys. Res. Space Physics*, *119*, 5328–5342, doi:10.1002/2014JA020064.

Miller, R. H., C. E. Rasmussen, T. I. Gombosi, G. V. Khazanov, and D. Winske (1993), Kinetic simulation of plasma flows in the inner magnetosphere, *J. Geophys. Res.*, *98*(A11), 19,301–19,313, doi:10.1029/93JA01292.

Moldwin, M. B. (1997), Outer plasmaspheric plasma properties: What we know from satellite data, *Space Sci. Rev.*, *80*(1–2), 181–198, doi:10.1023/A:1004921903897.

Ozhogin, P., P. Song, J. Tu, and B. W. Reinisch (2014), Evaluating the diffusive equilibrium models: Comparison with the IMAGE RPI field-aligned electron density measurements, *J. Geophys. Res. Space Physics*, *119*, 4400–4411, doi:10.1002/2014JA019982.

Pierrard, V., and J. F. Lemaire (2004), Development of shoulders and plumes in the frame of the interchange instability mechanism for plasmapause formation, *Geophys. Res. Lett.*, *31*, L05809, doi:10.1029/2003GL018919.

Pierrard, V., G. V. Khazanov, J. Cabrera, and J. Lemaire (2008), Influence of the convection electric field models on predicted plasmapause positions during magnetic storms, *J. Geophys. Res.*, *113*, A08212, doi:10.1029/2007JA012612.

Rasmussen, C. E., S. M. Guiter, and S. G. Thomas (1993), A two-dimensional model of the plasmasphere: Refilling time constants, *Planet. Space Sci.*, *41*(1), 35–43, doi:10.1016/0032-0633(93)90015-T.

Reinisch, B. W., X. Huang, P. Song, G. S. Sales, S. F. Fung, J. L. Green, D. L. Gallagher, and V. M. Vasyliunas (2001), Plasma density distribution along the magnetospheric field: RPI observations from IMAGE, *Geophys. Res. Lett.*, *28*(24), 4521–4524, doi:10.1029/2001GL013684.

Richards, P. G., and D. G. Torr (1990), Auroral modeling of the 3371Å emission rate: Dependence on characteristic electron energy, *J. Geophys. Res.*, *95*(A7), 10,337–10,344, doi:10.1029/JA095iA07p10337.

Richards, P. G., et al. (2000), On the relative importance of convection and temperature to the behavior of the ionosphere in North America during January 6–12, 1997, *J. Geophys. Res.*, *105*(A6), 12,763–12,776, doi:10.1029/1999JA000253.

Shue, J.-H., et al. (1998), Magnetopause location under extreme solar wind conditions, *J. Geophys. Res.*, *103*(A8), 17691–17700, doi:10.1029/98JA01103.

Singh, N., and K. S. Hwang (1987), Perpendicular ion heating effects on the refilling of the outer plasmasphere, *J. Geophys. Res.*, *92*(A12), 13,513–13,521, doi:10.1029/JA092iA12p13513.

Singh, N., and J. L. Horwitz (1992), Plasmasphere refilling: Recent observations and modeling, *J. Geophys. Res.*, *97*(A2), 1049–1079, doi:10.1029/91JA02602.

Song, P., and C. T. Russell (1992), Model of the formation of the low-latitude boundary layer for strongly northward interplanetary magnetic field, *J. Geophys. Res.*, *97*(A2), 1411–1420, doi:10.1029/91JA02377.

Spasojević, M., J. Goldstein, D. L. Carpenter, U. S. Inan, B. R. Sandel, M. B. Moldwin, and B. W. Reinisch (2003), Global response of the plasmasphere to a geomagnetic disturbance, *J. Geophys. Res.*, *108*(A9), 1340, doi:10.1029/2003JA009987.

Spiro, R. W., M. Harel, R. A. Wolf, and P. H. Reiff (1981), Quantitative simulation of a magnetospheric substorm 3. Plasmaspheric electric fields and evolution of the plasmapause, *J. Geophys. Res.*, *86*(A4), 2261–2272, doi:10.1029/JA086iA04p02261.

Su, Y.-J., J. E. Borovsky, M. F. Thomsen, R. C. Elphic, and D. J. McComas (2000), Plasmaspheric material at the reconnecting magnetopause, *J. Geophys. Res.*, *105*(A4), 7591–7600, doi:10.1029/1999JA000266.

Takahashi, K., S. Ohtani, R. E. Denton, W. J. Hughes, and R. R. Anderson (2008), Ion composition in the plasma trough and plasma plume derived from a Combined Release and Radiation Effects Satellite magnetoseismic study, *J. Geophys. Res.*, *113*, A12203, doi:10.1029/2008JA013248.

Titheridge, J. E. (1998), Temperatures in the upper ionosphere and plasmasphere, *J. Geophys. Res.*, *103*(A2), 2261–2277, doi:10.1029/97JA03031.

Tsyganenko, N. A. (1995), Modeling the Earth's magnetospheric magnetic field confined within a realistic magnetopause, *J. Geophys. Res.*, *100*(A4), 5599–5612, doi:10.1029/94JA03193.

Tsyganenko, N. A., G. Le, C. T. Russell, and T. Iyemori (1999), A study of the inner magnetosphere based on data of Polar, *J. Geophys. Res.*, *104*(A5), 10275–10283, doi:10.1029/1998JA900160.

Tu, J., P. Song, B. W. Reinisch, J. L. Green, and X. Huang (2006), Empirical specification of field-aligned plasma density profiles for plasmasphere refilling, *J. Geophys. Res.*, *111*, A06216, doi:10.1029/2005JA011582.

Tu, J., P. Song, B. W. Reinisch, and J. L. Green (2007), Smooth electron density transition from plasmasphere to the subauroral region, *J. Geophys. Res.*, *112*, A05227, doi:10.1029/2007JA012298.

Usanova, M. E., F. Darrouzet, I. R. Mann, and J. Bortnik (2013), Statistical analysis of EMIC waves in plasmaspheric plumes from Cluster observations, *J. Geophys. Res. Space Physics*, *118*, 4946–4951, doi:10.1002/jgra.50464.

Wang, Y., J. Tu, and P. Song (2015), A new Dynamic Fluid-Kinetic model for plasma transport within the plasmasphere, *J. Geophys. Res. Space Physics*, *120*, 8486–8502, doi:10.1002/2015JA021345.

Walsh, B. M., D. G. Sibeck, Y. Nishimura, and V. Angelopoulos (2013), Statistical analysis of the plasmaspheric plume at the magnetopause, *J. Geophys. Res. Space Physics*, *118*, 4844–4851, doi:10.1002/jgra.50458.

Walsh, B. M., T. D. Phan, D. G. Sibeck, and V. M. Souza (2014a), The plasmaspheric plume and magnetopause reconnection, *Geophys. Res. Lett.*, *41*, 223–228, doi:10.1002/2013GL058802.

Walsh, B. M., J. C. Foster, P. J. Erickson, and D. G. Sibeck (2014b), Simultaneous ground- and space-based observations of the plasmaspheric plume and reconnection, *Science*, *343*(6175), 1122–1125, doi:10.1126/science.1247212.

Wilson, G. R., J. L. Horwitz, and J. Lin (1992), A semikinetic model for early stage plasmasphere refilling: 1. Effects of Coulomb collisions, *J. Geophys. Res.*, *97*(A2), 1109–1119, doi:10.1029/91JA01459.